PERGAMON International Journal of Multiphase Flow 24 (1998) 1079–1103

International Journal of Multiphase Flow

Direct numerical simulation of droplet collisions in a turbulent channel flow. Part I: collision algorithm

M. Chen [a,*], K. Kontomaris [b], J.B. McLaughlin [a]

[a] *Department of Chemical Engineering, Clarkson University, Potsdam, NY 13699-5705, USA*
[b] *DuPont Central Research and Development, Experimental Station, Wilmington, DE 19880-0304, USA*

Received 10 February 1997; received in revised form 2 February 1998

Abstract

Fundamental understanding of the complex behavior of small droplets or particles in wall bounded turbulence and their interaction with the surrounding fluid is critical in a number of industrial processes. One approach for gaining valuable insight is the direct numerical simulation (DNS) of turbulence in conjunction with numerical computation of particle trajectories. Most previous work was limited to dilute suspensions of non-colliding particles. Part I of this paper extends previous methods by allowing for interparticle collisions. Part II presents results for the rate of collision between aerosol droplets.

Keywords: Droplet collisions; Direct numerical simulations

1. Introduction

An improved understanding of the behavior of small particles or droplets in wall-bounded turbulence could benefit the design and optimization of a wide variety of processes in the petroleum and chemical industries. The direct numerical simulation (DNS) of turbulence is a suitable research tool for elucidating some of the unresolved issues surrounding the behavior of dilute suspensions of small particles at low Reynolds numbers. A recent review by McLaughlin (1994) discusses the strengths and limitations of this approach.

The first goal of this work was to extend previous methods of particle tracking in DNS by incorporating interparticle collisions. This allows the application of such methods to higher concentrations of the particulate phase. Part I describes an algorithm for simulating the

* Corresponding author.

0301-9322/98/$19.00
PII: S0301-9322(98)00007-X

dispersion of small coalescing and depositing droplets in a turbulent channel flow. The flow Reynolds number, based on the hydraulic diameter and the bulk velocity, was 7050. The effect of the droplets on the turbulence of the carrier gas was neglected.

Most previous work has been limited to very dilute suspensions of non-interacting particles. The recent work by Sundaram and Collins (1994), who studied collision statistics in a DNS of a particle-laden isotropic flow, is an exception. Also related is the work of Lavieville et al. (1995) who studied the behavior of colliding particles in a large eddy simulation of isotropic turbulence. This paper extends a previous particle tracking algorithm to allow for interparticle collisions.

Chen et al. (1995) have previously offered a brief description of the algorithm and some preliminary results. In a typical run, a large number of droplets of a given size are released in the simulated channel flow at random positions according to a uniform distribution. At the time of the release, the channel flow is stationary and fully-developed. In the absence of particle feedback effects, it remains stationary and fully-developed for the duration of a run. Then, the evolution of the fluctuating three-dimensional gas flow field and the droplet trajectories are calculated for a prescribed length of time by integrating the governing equations of motion.

The review by McLaughlin (1994) pointed out some of the uncertainties in calculating the hydrodynamic force exerted on a dispersed particle. Notwithstanding the difficulties in formulating an exact equation of motion, the study of simulated behavior in turbulent flows has provided valuable information that is very difficult to obtain experimentally.

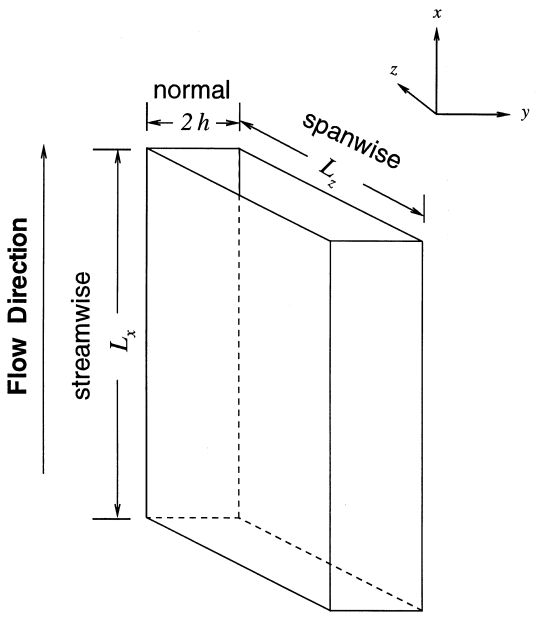

Fig. 1. Channel flow geometry.

Drag, lift, Brownian, and gravitational forces on the droplets are accounted for. However, for the range of conditions examined in this work, the effect of Brownian and gravitational forces was negligible.

Collisions are detected as a geometric interception of droplet trajectories. All interdroplet collisions are assumed to lead to instantaneous coalescence. Droplets approaching either of the channel walls to within the mean free path of the molecules of the surrounding gas are considered deposited and they are removed from the simulation. The accuracy and computational efficiency of the algorithm are discussed.

2. Methodology

2.1. Turbulent channel flow

A statistically stationary, fully-developed, isothermal flow of a Newtonian fluid bounded by two vertical and parallel flat walls was considered. The channel walls were assumed rigid and smooth. The flow geometry and the coordinate system used in the simulation are shown in Fig. 1. The origin of the coordinate system is located on the centerline, and the x, y and z axes point in the streamwise, normal, and spanwise directions, respectively. The walls confining the flow were of infinite extent and at rest with respect to the coordinate system. The flow was assumed to be incompressible and it was driven by a constant mean pressure gradient.

The velocity of the fluid was obtained by a numerical solution of the Navier–Stokes equation:

$$\frac{\partial \mathbf{u}^+}{\partial t^+} + \mathbf{u}^+ \cdot \vec{\nabla} + \mathbf{u}^+ = - \vec{\nabla} + p^+ + \nabla^{+2}\mathbf{u}^+. \tag{1}$$

In (1), all physical quantities are made dimensionless in terms of the friction velocity, u^*, the kinematic viscosity of the fluid, v, and the fluid density, ρ_f. A " + " superscript denotes a dimensionless quantity. The symbols $\mathbf{u}^+$, p^+ and t^+ denote the dimensionless fluid velocity, the dimensionless hydrodynamic pressure and the dimensionless time. The friction velocity, u^*, is defined by

$$u* = \sqrt{\frac{|\tau_w|}{\rho_f}} \tag{2}$$

where τ_w is the wall shear stress. Table 1 lists various physical parameters characteristic of the wall region which are used throughout this work to scale the reported results. In Table 1, m_p denotes the mass of a droplet.

Table 1
Nondimensionalization Factors

Velocity	Length	Time	Acceleration	Force
u^*	v/u^*	v/u^{*2}	u^{*3}/v	$m_p u^{*3}/v$

The fluid was assumed to be incompressible

$$\vec{\nabla} \cdot \mathbf{u}^+ = 0. \tag{3}$$

Periodic boundary conditions were imposed in the downstream and spanwise directions, with periods L_x and L_z, respectively. Rigid, no-slip boundary conditions were imposed on the channel walls:

$$\mathbf{u}^+ = 0, \qquad Y = h^+, -h^+, \tag{4}$$

where h is the channel half width and Y denotes the dimensionless value of y. (The symbol y^+ will be used to denote the distance measured from the closest channel wall.)

The Navier–Stokes equation was integrated in time using a fractional time-stepping method. All hydrodynamic fields were discretized within a domain of size $L_x \times 2\,h \times L_z$ using pseudospectral methods. Fourier series were used in the downstream and spanwise directions. Chebyshev polynomials were used in the direction normal to the walls. The numerical techniques that were used to perform the simulations of the channel flow have been described by Lyons et al. (1991) and Chen and McLaughlin (1995).

2.2. Droplet tracking

2.2.1. Droplet equation of motion

The computation of the trajectories of a polydisperse suspension of small spherical droplets was based on a numerical integration of their equation of motion:

$$\frac{\mathrm{d}\mathbf{V}^+}{\mathrm{d}t^+} = C_\mathrm{D}\mathbf{F}_\mathrm{d}^+ + \mathbf{F}_\mathrm{b}^+ + \mathbf{F}_\mathrm{l}^+ - g^+\hat{x}, \tag{5}$$

where $\mathbf{V}$ is the droplet Lagrangian velocity, t is the time, g is the acceleration of gravity, and $\hat{x}$ denotes a unit vector in the x-direction. All quantities were made dimensionless with the friction velocity, the kinematic viscosity of the gas, and the mass of the droplet. The correlation suggested by Clift et al. (1978) was used to compute the coefficient C_D. For values of the droplet Reynolds number, Re_p, less than 0.01, the Proudman–Pearson result was used to compute C_D:

$$C_\mathrm{D} = 1 + \frac{3}{16} Re_\mathrm{p}. \tag{6}$$

For $0.01 < Re_\mathrm{p} < 20$,

$$C_\mathrm{D} = 1 + 0.1315 Re^{0.82-05w}, \tag{7}$$

where $w = \log_{10} Re_\mathrm{p}$.

According to (5), contributions to the acceleration of a droplet of unit mass are made by the wall-corrected drag ($C_\mathrm{D}\mathbf{F}_\mathrm{d}$), Brownian ($\mathbf{F}_\mathrm{b}$), lift ($\mathbf{F}_\mathrm{l}$), and gravity forces. The coefficient C_D corrects the Stokes drag force to account for inertial effects at non-negligible droplet Reynolds numbers. Methods for incorporating the effects of instantaneous collisions on droplet trajectories are discussed in the following section.

A detailed discussion of the forces in (5) may be found in Chen and McLaughlin (1995). Briefly, the drag force includes wall corrections and molecular slip effects. The latter effects are accounted for by the Cunningham slip factor, which is defined as follows:

$$C_c = 1 + \frac{2\lambda_m}{d}[1.257 + 0.4e^{-0.55d/\lambda_m}], \tag{8}$$

where d is the particle diameter and λ_m is the molecular mean free path. The dimensionless particle relaxation time, τ, is a useful way of characterizing particle inertia. It is defined by

$$\tau^+ = C_c \frac{(2S+1)d^{+2}}{36} \tag{9}$$

where S is the particle–fluid density ratio.

The particle equation of motion in (5) is considered valid everywhere along the trajectory of a droplet (particle) except at the instants of collisions where the droplet velocity changes discontinuously. As two droplets approach within a few radii, the hydrodynamic force exerted on each droplet is affected by the influence of the disturbance flow field of the other. The form of the hydrodynamic forces in (5) does not account for hydrodynamic interaction between droplets. Although the suspensions to be considered are dilute, hydrodynamic interactions can be significant when two droplets approach each other. Marble (1964) and Sundarajakumar and Koch (1996) have discussed the conditions under which the hydrodynamic interaction can be neglected. In this paper, all simulations are initiated with monodisperse droplets. Coalescence of droplets can produce some doublets and triplets. However, the vast majority of the droplets were singlets in all the calculations to be reported. Finally, the possibility of a force field surrounding a droplet (electrostatic, Van der Waals, etc.) was not considered, and any effects of droplet rotation, internal circulation, or lubrication forces at close proximity were also neglected.

2.2.2. Evaluation of fluid velocities at droplet positions

The calculation of the drag and lift forces appearing in (5) requires the evaluation of the undisturbed fluid velocity at the instantaneous droplet positions. The DNS supplies the Eulerian velocity values on a three-dimensional grid. Since the instantaneous position of a droplet does not, in general, coincide with a grid point, an interpolation of the Eulerian velocity at the droplet locations is needed.

An accurate evaluation of droplet velocities is critical for studying collisions because these depend on the often small relative droplet velocity. One source of error is the use of interpolated fluid velocities. Several methods, such as direct summation (DS), partial Hermite interpolation (PHI), Lagrangian interpolation (LGI) and linear interpolation (LNI), can be used to obtain the fluid velocity at the droplet location. Yeung and Pope (1988), Balachandar and Maxey (1989), and Kontomaris et al. (1992) studied the accuracy of different interpolation methods relative to a direct summation of the spectral Fourier series which provides velocity values as accurate as the DNS itself. Partial Hermite interpolation was found to provide acceptable accuracy at a much lower computational cost than direct summation.

In this paper, partial Hermite interpolation method was used to obtain the fluid velocity at a droplet's location. The effect of interpolation errors on the observed collision rate is assessed in a later section.

2.2.3. Droplet displacement

The particle trajectories are viewed as a succession of small increments. Except on the first time step, a second order Adams (explicit) method was used to compute the increments. It takes the form:

$$\mathbf{X}_{n+1} = \mathbf{X}_n + [c_1\mathbf{V}_{n+1} - c_2\mathbf{V}_n]\Delta t, \tag{10}$$

where $\mathbf{X}$ and $\mathbf{V}$ denote the droplet location and velocity, respectively. The subscripts "n" and "$n + 1$" denote the time at the beginning of the nth time step and the end of the nth time step, respectively, and c_1 and c_2 are constants (Adams algorithm factors). On the first two time steps, the latter constants are 1 and 0, respectively. Thereafter, they are equal to 1.5 and 0.5, respectively. The time step for the integration of the equation of particle motion was equal to that used for the integration of the flow equations.

2.2.4. Initial droplet placement

The initial allocation of droplets is specified according to the objective of a run. For the runs reported in Part II, droplets were released at random positions throughout the channel. In all cases, the volume fraction of the dispersed phase was sufficiently small that the probability of two droplets overlapping was insignificant. The initial coordinates of the droplets satisfied the following condition:

$$(0, -h + d/2, 0) \leq \mathbf{X}_0 \leq (L_x, h - d/2, L_z). \tag{11}$$

Droplets are always confined within the computational domain by recycling droplets exiting in the periodic directions. At the initial time, the velocities of the droplets were set equal to the unoccupied local fluid velocities at the droplet locations. Isokinetic injection simulates the case of droplet precipitation from the gas phase, assuming that the droplet size is not much larger than the nuclei. Thereafter, the droplet motion was governed by its equation of motion. To obtain a trajectory, the droplet equation of motion was integrated simultaneously with the Navier–Stokes equation.

2.2.5. Simulation of interdroplet collisions

The tracking algorithm discussed in the previous subsection is suitable only for non-interacting droplets (particles). In this subsection, it is extended to incorporate the effects of interdroplet collisions on individual droplet trajectories as has been previously described by Chen et al. (1995). Lavieville et al. (1995) have also presented a method for incorporating particle collisions in a large eddy simulation of isotropic turbulence based on an adaptation of an earlier algorithm by Hopkins and Louge (1991). Finally, Sundaram and Collins (1996) have examined, in some detail, the numerical aspects of simulating the motion of suspensions of finite-volume particles in DNS of isotropic turbulence. Related experience can also be drawn from considerations of the more general problem of collisions between objects of arbitrary (and often changing) shapes in simulated motion relative to each other and to stationary

objects or boundaries. This problem is of common interest to a number of diverse fields including molecular dynamics, particle dynamics and granular mechanics, computer animation of dynamic systems or virtual interactive environments, and robotics. The methodology for detecting contacts remains similar despite the various origins of relative object motion which range from prescribed dynamic laws of varying degrees of complexity to completely arbitrary forcing specified interactively.

The effect of particle acceleration resulting from the interaction with the surrounding fluid and gravity is accounted for at a sequence of discrete times, t_n, uniformly spaced at time intervals, Δt. Between successive time instants, $[t_n,\ t_{n+1}]$, the trajectories of the particles are fully determined by their known initial locations, $\mathbf{X}_n$, and velocities, $\mathbf{V}_n$. Therefore, particle pairs that are on a collision course can be identified and the anticipated discontinuous change in their velocities and trajectories at impact can be used to determine their positions and velocities at the end of a time step. The alternative approach of retroactively correcting for collisions in the previous time step when particles are found to overlap can seriously underestimate the collision rate for a comparable time step size (Sundaram and Collins, 1996). Consideration is restricted to binary collisions because the likelihood of multiple simultaneous contacts in dilute suspensions of instantaneously colliding particles is negligible. Fig. 2 shows the sequence of steps followed in simulating trajectories of colliding particles.

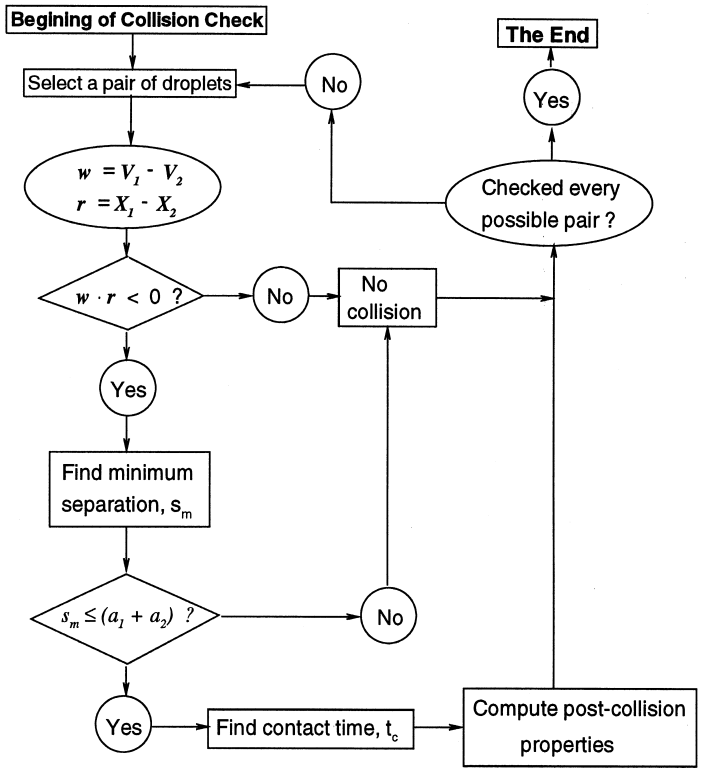

Fig. 2. Collision algorithm.

2.2.6. Identification of likely collision partners

Within a small time interval, Δt, only collisions between neighboring particles are likely. Substantial computational savings can result from eliminating remote particles from the search for collision pairs. One approach for designating neighbors of a given particle is to maintain a list of other particles located within an appropriately chosen distance. This approach is efficient for suspensions of a few slowly moving particles for which the required neighbor lists are short and need to be updated only infrequently (Hogue and Newland, 1994; Sundaram and Collins, 1996). In rapidly dispersing suspensions involving a large number of particles, it is more efficient to partition the domain of interest and reduce the search space to only neighboring cells.

In general, one could divide the computational domain into $\kappa_x\kappa_y\kappa_z$ non-overlapping slices of a uniform size $(L_x/\kappa_x) \times (2\,h/\kappa_y) \times (L_z/\kappa_z)$. The search for collision partners for a given particle would be limited to the subset of other particles in the same or any of the surrounding 26 slices. In this work, a simpler strategy was used. The channel was divided into $\kappa_x\kappa_z$ non-overlapping slices. Thus, the search for collision partners was limited to the particle containing and the surrounding eight slices. The reason for using a two-dimensional partition was that large accumulations of droplets occurred in some of the runs to be discussed and, as a result, the memory requirements for the partitioning would have been too large. The choice of spacing for the collision search lattice is discussed in the section on simulation procedures.

2.2.7. Minimum particle separation within a time step

The absence of particle acceleration within a time step leads to constant particle velocities before collisions and allows collision detection from purely kinematic and geometric considerations. Fig. 3 depicts a pair of particles (droplets) in free-flight originating at time t_n from known positions and with known velocities. It is convenient to describe the relative particle motion in a frame of reference, x'–y', with its origin on one of the two approaching particles, say P_2, and its x'-axis anti-parallel to their relative velocity,

$$\mathbf{w}_n = \mathbf{V}_{1n} - \mathbf{V}_{2n}, \tag{12}$$

where $\mathbf{V}_{1n}$ and $\mathbf{V}_{2n}$ are the velocities in the laboratory of particle 1 (P_1) and particle 2 (P_2), respectively, in the nth time step. The y'-axis lies on the plane defined by the vectors, $\mathbf{w}_n$ and $\mathbf{r}_n$. The particle separation vector $\mathbf{r}_n$ is defined by

$$\mathbf{r}_n = \mathbf{X}_{1n} - \mathbf{X}_{2n}, \tag{13}$$

where $\mathbf{X}_n$ and $\mathbf{X}_{2n}$ are the coordinates of P_1 and P_2 at the end of the nth time step in the laboratory frame. The relative motion of the two particles is confined to the x'–y' plane and its trajectory is a straight line parallel to the x'-axis. Fig. 3 shows that the closest possible approach , s_m, of the centers of the two particles is

$$s_\mathrm{m} = r_n \sin\theta, \tag{14}$$

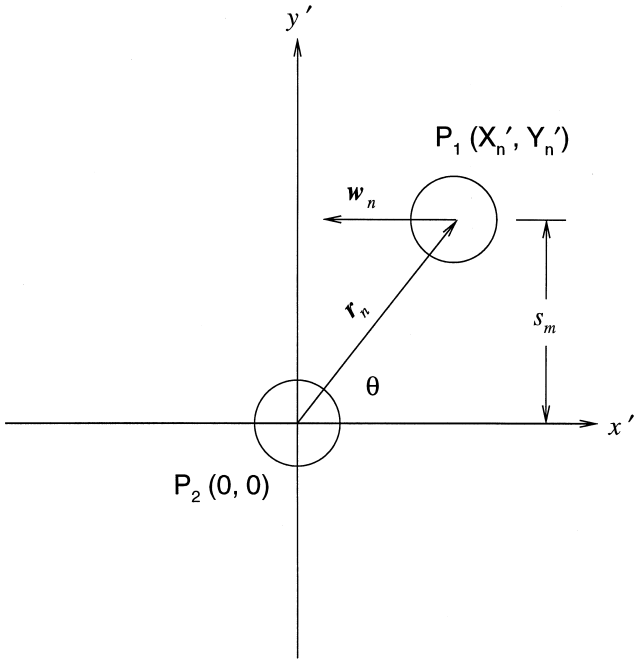

Fig. 3. Coordinate system for relative motion of droplet pairs.

where

$$\theta = \cos^{-1}\left(\frac{\mathbf{r}_n \cdot \mathbf{w}_n}{r_n w_n}\right) \qquad 0 \le \theta \le \pi. \tag{15}$$

The magnitudes of the relative velocity and separation vectors are denoted by w_n and r_n, respectively. The moment of closest approach, t_m, occurs when the center of P_1 crosses the y'-axis (see Fig. 3). It is given by

$$t_m = t_n + \frac{r_n \cos\theta}{w_n}. \tag{16}$$

The above results were also obtained by Chen et al. (1995) and Sundaram and Collins (1996) from a minimization of the magnitude of the particle separation distance. If the motion of the two particles were allowed to continue uninterrupted, the variation of their separation vector from its initial value at t_n could be expressed analytically in terms of their constant relative velocity as

$$\mathbf{r}(t) = \mathbf{r}_n + (t - t_n)\mathbf{w}_n. \tag{17}$$

Therefore, the particle separation distance would vary as

$$r(t) = \sqrt{r_n^2 + 2[\mathbf{r}_n \cdot \mathbf{w}_n](t - t_n) + w_n^2(t - t_n)^2}. \tag{18}$$

Minimization of the functional representation of $r(t)$ based on the condition

$$\frac{\partial r(t)}{\partial t} = 0 \qquad \text{at} \quad t = t_{\mathrm{m}} \tag{19}$$

leads to the evaluation of the time at which the particle separation distance is a minimum:

$$t_{\mathrm{m}} = t_n - \frac{\mathbf{r}_n \cdot \mathbf{w}_n}{w_n^2} \tag{20}$$

and the minimum separation is given from (18) as

$$s_{\mathrm{m}} = r(t_{\mathrm{m}}). \tag{21}$$

It should be noted that condition (19) does not constrain the time interval within which a minimum is sought. It can be easily verified that these results are identical to (16) and (14) obtained from a geometrical interpretation of the collision encounter.

The time of the closest approach, t_{m}, determined from (16) or (20) does not necessarily fall within the current time step. The instant of minimum separation within $[t_n, t_{n+1}]$, t^*_{m}, can be determined with the aid of Fig. 4, which depicts the possible trajectories of the relative motion of a particle pair over the time interval of interest, in the transformed frame of reference $x'y'$. The trajectories are straight lines anti-parallel to the x'-axis, fully characterized by the initial coordinates, $\mathbf{X}_n$, and final coordinates, $\mathbf{X}_{n+1}$, of particle P_1. Three cases are identified: in case A, the particles are moving apart from each other throughout the current time step; therefore, $t^*_{\mathrm{m}} = t_n$. In case B, the particles are moving toward each other throughout the duration of the

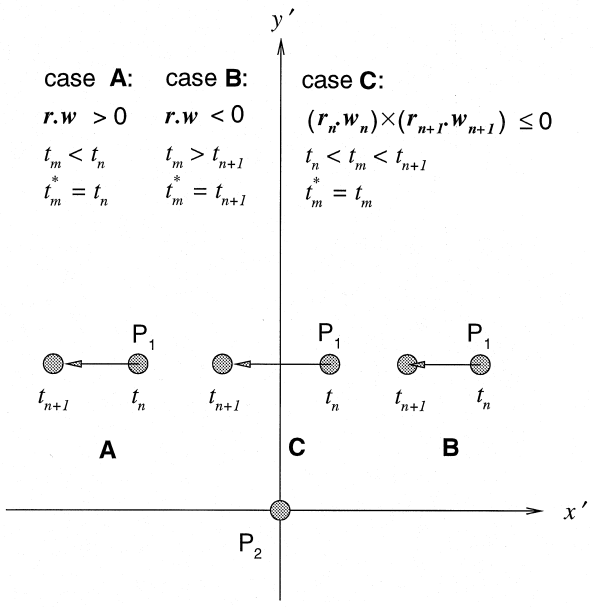

Fig. 4. Relative droplet motion over a time step.

current time step. Therefore, they are the closest at the end of the current time step, which gives$t^*_m = t_{n+1}$. Finally, in case C, the particles achieve a minimum separation at time $t^*_m = t_m$ between t_n andt_{n+1}. The x' coordinate of P_1 changes from positive to negative. The time to minimum separation within a time step for all these cases can be expressed compactly as (Sundaram and Collins, 1996)

$$t*_m = t_n + H(t_m - t_n)[t_m - t_n + (t_{n+1} - t_m)H(t_m - t_{n+1})], \tag{22}$$

where H is the Heaviside function. In all cases, the minimum separation distance within the current time step is

$$s*_m = r(t*_m). \tag{23}$$

2.2.8. Contact detection

Contacts between neighboring particles within a time step are detected by determining whether their minimum separation becomes less than or equal to the sum of their radii:

$$s*_m \leq d_{12}, \tag{24}$$

where

$$d_{12} = \frac{d_1 + d_2}{2}. \tag{25}$$

A value of $s^*_m = 0$ indicates a head on collision; eccentric collisions correspond to positive values for s^*_m. When $s^*_m = d_{12}$, the droplets just touch each other.

For pairs that collide, the exact moment of contact, t_c, is determined by solving the equation

$$r(t_c) - d_{12} = 0. \tag{26}$$

The two roots of the above equation are

$$t_c = t_n - \frac{\mathbf{r}_n \cdot \mathbf{w}_n}{w_n^2}\left(1 \pm \sqrt{1 - K_n}\right) \tag{27}$$

where

$$K_n = \frac{r_n^2 w_n^2}{(\mathbf{r}_n \cdot \mathbf{w}_n)^2}\left(1 - \frac{d_{12}^2}{r_n^2}\right). \tag{28}$$

The relative velocity and separation vectors in the above expressions are calculated at $t = t_n$. For colliding particles, both roots of (27) are real. This may be shown by using the fact that

$$(\mathbf{r}_n \cdot \mathbf{w}_n)^2 - w_n^2 r_n^2 + w_n^2 d_{12}^2 = w_n^2(d_{12}^2 - r_n^2 \sin^2\theta). \tag{29}$$

For a collision to occur, the right hand side of (29) must be non-negative. Thus, both roots of (27) must be real. The choice between the two roots becomes clear when (27) is rewritten as

$$t_c = t_m \pm \frac{\mathbf{r}_n \cdot \mathbf{w}_n}{w_n^2}\sqrt{1 - K_n}. \tag{30}$$

The time of contact, t_c, in general, precedes the time of minimum separation, t_m, because the calculation of t_m allows particles to interpenetrate. To satisfy the requirement that $t_c \leq t_m$, given that $\mathbf{r}_n \cdot \mathbf{w}_n \leq 0$, the plus sign is selected in the above equation. For droplets which move tangentially at contact, $t_c = t_m$. The minus sign corresponds to the final instant of contact after imaginary interpenetration of the two spheres.

The coordinates of the centers of the particles at the instant of collision can be determined by

$$\mathbf{X}_c = \mathbf{X}_n + (t_c - t_n)\mathbf{V}_n. \tag{31}$$

2.2.9. Droplet coalescence

It was assumed that two droplets would combine instantaneously upon contact to form a larger spherical droplet. For equal size droplets, the center of the child droplet is at the midpoint of the line between the centers of the parent droplets. Fig. 5 schematically illustrates the coalescence of two droplets. The outcome of a collision can be determined from conservation of mass and conservation of momentum. Kinetic energy is not conserved during coalescence. Conservation of mass was used to calculate the size of the child droplet:

$$d_3 = \sqrt[3]{d_1^3 + d_2^3}, \tag{32}$$

where it was assumed that the density of the child droplet is the same as that of the parents.

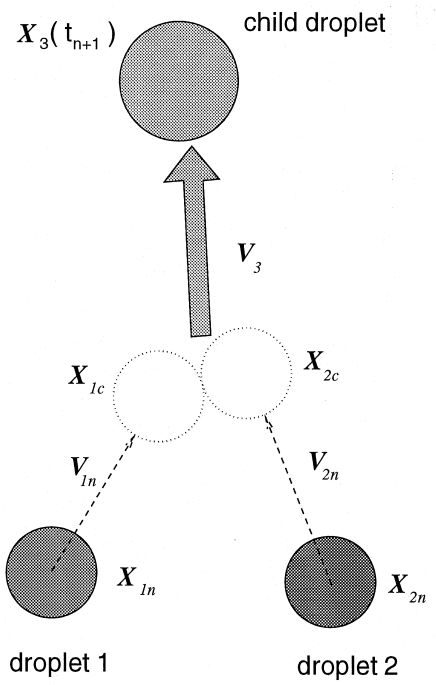

Fig. 5. Schematic illustration of droplet coalescence.

Conservation of translational momentum was applied to obtain the velocity of the child droplet:

$$m_1\mathbf{V}_1 + m_2\mathbf{V}_2 = m_3\mathbf{V}_3. \tag{33}$$

In (33), subscripts "1" and "2" denote the parent droplets, the subscript "3" denotes the child droplet, m is the droplet mass, and $\mathbf{V}$ is the droplet velocity. After the collision, the child droplet will have the following velocity:

$$\mathbf{V}_3 = \frac{\mathbf{V}_1 d_1^3 + \mathbf{V}_2 d_2^3}{d_3^3}. \tag{34}$$

The position of the child droplet at the end of the current time step is expressed as follows:

$$\mathbf{X}_3(t_{n+1}) = \frac{\mathbf{X}_{1c} + \mathbf{X}_{2c}}{2} + (t_{n+1} - t_c)\mathbf{V}_3, \tag{35}$$

where $\mathbf{X}_{1c}$ and $\mathbf{X}_{2c}$ denote the coordinates of P_1 and P_2 at the moment of the collision, respectively.

The assumption of coalescence used in this work can be replaced with rules prescribing other types of impact dynamics. For example, elastic collisions between rigid or deformable particles with smooth or rough surfaces could be simulated. One could also assign a probability of coalescence.

The omission of hydrodynamic droplet-droplet interactions which is equivalent to an assumption of perfect capture efficiency (also made by Saffman and Turner, 1956) may lead to a significant overestimation of the collision rates for smaller droplets. Multiple collisions of a droplet within a time step were also neglected. This may introduce some errors in the collision rate. However, the error is small for small mass loadings (volume fractions) and small time steps.

2.3. Simulation of droplet-wall collisions

In the simulations to be reported, the criterion of the wall deposition of droplets was

$$\delta^+ \leq \lambda_m^+, \tag{36}$$

where δ^+ is the dimensionless gap between the droplet and the nearest wall. At this separation, continuum mechanics is no longer valid, which means that the wall-drag corrections used in the droplet equation of motion are not valid. Furthermore, it is likely that the Van der Waals attraction between the droplet and the wall will cause deposition at this separation.

In the simulations, it was also assumed that the droplets wet the walls if they deposit on the walls. The possibility of splashing caused by inertial droplet–wall collisions was not considered. Deposited droplets were permanently removed from the calculation. The possibility of re-entrainment was not allowed for. As a result, the channel was gradually depleted of droplets.

3. Simulation procedures

3.1. Physical parameters

The independent input parameters defining a numerical experiment are the properties of the fluid (temperature, T, pressure, p, density, ρ_f, kinematic viscosity, v, and molecular diameter, σ_m), the flow variables (channel width, $2h$, and bulk velocity, u_b), and the properties of the particle phase (droplet diameter, d, droplet density, ρ_p, and initial droplets volume fraction, ϕ_0). The fluid properties were fixed for all the simulations at the values listed in Table 2 which correspond to air at ambient conditions.

The fluid molecular mean free path is needed for the Cunningham slip correction. It is calculated from the kinetic theory of gases:

$$\lambda_m = \frac{1}{\sqrt{2}\pi\sigma_m{}^2 n_m}, \tag{37}$$

where the molecular number density is given by

$$n_m = \frac{N_A P}{RT} \tag{38}$$

with $N_A = 6.023 \times 10^{23}$ mol^{-1}, $R = 82.057$ cm^3 atm/(mol·K).

A Reynolds number, Re, based on the bulk velocity and the hydraulic radius, $R_h = h$, can be calculated as

$$Re = \frac{4R_h u_b}{v}. \tag{39}$$

The friction velocity is then calculated as

$$u* = \left(\frac{|\tau_w|}{\rho_f}\right)^{1/2}, \tag{40}$$

where

$$|\tau_w| = \left|\frac{dP}{dx}\right| h, \tag{41}$$

and

$$\left|\frac{dP}{dx}\right| = f\frac{1}{2}\rho_f u_b^2 \frac{1}{R_h}. \tag{42}$$

The friction factor, f, is given by the Blasius correlation:

$$f = \frac{0.0791}{Re^{0.25}}, \tag{43}$$

for $Re < 10^5$. The wall length and time scales are then calculated as $l* = v/u*$ and $t* = v/u*^2$. The channel half-width in wall units is equal to $h^+ = h/l*$.

Table 2a
Input parameters for the fluid (ambient air) and the flow conditions

P (atm)	T (K)	ν (cm^2/s)	ρ_f (g/cm^3)	σ_m (Å)	u_b (m/s)	$2h$ (mm)
1	298	0.15	1.12×10^{-3}	3.6	11.42	4.63

Table 2b
Calculated flow parameters

λ_m	Re	u^*	l^*	t^*	h^+
0.07 μm	7050	75 cm/s	20 μm	26.67 μs	125

Application to the case of flow of air at ambient conditions (see Table 2a) yields a value of $\lambda_m = 0.07\ \mu m$ for the molecular mean free path. For $u_b = 11.42$ m/s and $2h = 4.63$ mm, the channel Reynolds number becomes $Re = 7050$, yielding a friction velocity $u^* = 75$ cm/s and wall length and time scales equal to 20 μm and 26.67 μs, respectively. Therefore, the channel half-width in wall units is equal to $h^+ = 125$. Table 2b summarizes the calculated flow parameters. Simulation results for this set of conditions are reported in Part II of this paper.

The three primary variables characterizing the droplet phase (d, ρ_p, and ϕ_0) for each run can be used to calculate a number of other variables to guide the choice of computational parameters and facilitate the interpretation of results. These include the droplet-to-fluid density ratio, $S = \rho_p/\rho_f$, the initial number concentration of droplets, C_0, the particle relaxation time, the Schmidt number based on the Brownian particle diffusivity, the Cunningham correction factor, and the number concentration in wall units.

The initial particle number density, C_0, is calculated from the known particle volume fraction as

$$C_0 = \frac{\phi_0}{V_p}, \tag{44}$$

where

$$V_p = \frac{\pi}{6} d^3 \tag{45}$$

is the droplet volume. The initial droplet mass loading, m_l, is calculated as

$$m_l = \frac{\phi_0 S}{1 - \phi_0}. \tag{46}$$

An estimate of the initial mean droplet separation, S_d, is obtained as

$$S_d = d\left(\left(\frac{\phi_{max}}{\phi_0}\right)^{1/3} - 1\right), \tag{47}$$

where, for a cubic array of spherical particles, $\phi_{max} = \pi/6$. Expressions for the Cunningham slip

Table 3
Input parameters for the droplet phase for the various simulation runs reported in Part II

Run ID	d (μm)	S	ϕ_0
Re = 7050			
1	3.09	713	5.84×10^{-6}
2	4.4	713	1.69×10^{-5}
3	5.42	30	2.10×10^{-5}
4	5.42	100	2.10×10^{-5}
5	5.42	713	3.15×10^{-5}
6	7.78	713	9.32×10^{-5}
7	8.99	713	1.44×10^{-4}
8	9.96	20	1.30×10^{-4}
9	9.96	100	6.52×10^{-5}
10	9.96	142.6	6.52×10^{-5}
11	9.96	213.9	6.52×10^{-5}
12	9.96	300	6.52×10^{-5}
13	9.96	713	1.30×10^{-4}
14	9.96	1100	3.26×10^{-5}
15	9.96	2000	3.26×10^{-5}
16	14.1	713	1.89×10^{-4}
17	16.8	100	1.56×10^{-4}
18	16.8	300	1.56×10^{-4}
19	16.8	713	6.26×10^{-5}
20	16.8	713	1.56×10^{-4}
21	16.8	713	2.19×10^{-4}
22	16.8	713	3.13×10^{-4}
23	16.8	1273	1.56×10^{-4}

factor, the particle relaxation time, and the Schmidt number were given in Section 2. The single particle terminal velocity in quiescent fluid was calculated as

$$V_t = \tau\left(1 - \frac{1}{S}\right) g/C_D \approx \tau g/C_D \tag{48}$$

for heavy droplets in a gas.

The range of values for the parameters of the droplet phase for the simulations in Part II of this paper are listed in Table 3. Instead of the droplet density, Table 3 gives the droplet-to-fluid density ratio, $S = \rho_p/\rho_f$. The value $S = 713$ corresponds to olive oil droplets in air under ambient conditions. Other calculated parameters for the droplet phase are summarized in Table 4 (where S_k is the Schmidt number).

3.2. Computational parameters

Once one specifies the physical parameters of a simulation, the numerical parameters are largely determined by accuracy, stability, and computational efficiency considerations. A stationary, fully-developed velocity field is used to start the channel flow simulation. The required channel flow numerical parameters include the periods in the x and z directions, L_x

Table 4
Calculated parameters for the droplet phase for the various simulations reported in Part II

Run ID	$C_0(\mathrm{cm}^{-3})$	m_l	S_d^+	d^+	C_c	τ^+	V_r^+	Sc
1	3.78×10^5	0.0042	6.76	0.155	1.057	1.0	3.48×10^{-4}	1.69×10^6
2	3.78×10^5	0.0120	6.69	0.220	1.040	2.0	6.94×10^{-4}	2.44×10^6
3	2.52×10^5	0.0006	7.65	0.271	1.032	0.126	4.26×10^{-5}	3.03×10^6
4	2.52×10^5	0.0021	7.65	0.271	1.032	0.421	1.45×10^{-4}	3.03×10^6
5	3.78×10^5	0.0225	6.65	0.271	1.032	3.0	1.05×10^{-3}	3.03×10^6
6	3.78×10^5	0.0665	6.53	0.389	1.023	6.0	2.13×10^{-3}	4.39×10^6
7	3.78×10^5	0.1027	6.46	0.450	1.020	8.0	2.84×10^{-3}	5.09×10^6
8	2.52×10^5	0.0026	7.43	0.498	1.018	0.280	9.29×10^{-5}	5.65×10^6
9	1.26×10^5	0.0065	9.47	0.498	1.018	1.40	4.84×10^{-4}	5.65×10^6
10	1.26×10^5	0.0093	9.47	0.498	1.018	2.0	6.93×10^{-4}	5.65×10^6
11	1.26×10^5	0.0139	9.47	0.498	1.018	3.0	1.04×10^{-3}	5.65×10^6
12	1.26×10^5	0.0196	9.47	0.498	1.018	4.2	1.46×10^{-3}	5.65×10^6
13	2.52×10^5	0.0927	7.43	0.498	1.018	10.0	3.48×10^{-3}	5.65×10^6
14	6.30×10^4	0.0359	12.07	0.498	1.018	15.4	5.37×10^{-3}	5.65×10^6
15	6.30×10^4	0.0652	12.07	0.498	1.018	28.0	9.78×10^{-3}	5.65×10^6
16	1.26×10^5	0.1348	9.20	0.705	1.012	20.0	6.94×10^{-3}	8.04×10^6
17	6.30×10^4	0.0156	11.74	0.840	1.010	4.0	1.37×10^{-3}	9.60×10^6
18	6.30×10^4	0.0468	11.74	0.840	1.010	12.0	4.13×10^{-3}	9.60×10^6
19	2.52×10^4	0.0446	16.21	0.840	1.010	28.0	9.84×10^{-3}	9.60×10^6
20	6.30×10^4	0.1112	11.74	0.840	1.010	28.0	9.84×10^{-3}	9.60×10^6
21	8.82×10^4	0.1562	10.39	0.840	1.010	28.0	9.84×10^{-3}	9.60×10^6
22	1.26×10^5	0.2232	9.13	0.840	1.010	28.0	9.84×10^{-3}	9.60×10^6
23	6.30×10^4	0.1986	11.74	0.840	1.010	50.0	1.76×10^{-2}	9.60×10^6

and L_z, the numbers of grid points in the x, y and z directions, N_x, N_y and N_z, and the time step, Δt. Recommended values of these parameters are listed in Table 5.

The work of Lyons et al. (1991) and others for single phase channel flow indicated that the downstream and spanwise periods should be several times larger than the channel width. This is necessary to describe the largest eddies that contain a significant amount of energy. Since turbulence structures in the wall region tend to be elongated in the downstream direction, previous workers have generally used a larger period in the x direction than in the z direction. However, in a simulation for $Re = 7050$, McLaughlin (1989) chose the spanwise period to be equal to downstream period. This was because the downstream period was unusually short (630 wall units) relative to the channel width (250 wall units) and it was desirable that the spanwise period length should be much larger than the spanwise streak spacing (100 wall units). In spite of the small downstream period, his turbulence intensities agreed well with results of simulations with much larger periods in the viscous wall region. Thus, his computational box size was used in the simulations at $Re = 7050$ reported in Part II.

Table 5
Numerical Parameters for channel flow simulations at a low Reynolds number

Re	L_x^+	h^+	L_z^+	N_x	N_y	N_z	Δx^+	Δy^+	Δz^+	Δt^+
7050	630	125	630	16	65	64	39.4	0.15-6.13	9.84	0.25

One must consider the accuracy of particle trajectories as well as the accuracy of turbulence statistics when selecting grid spacings. In Table 5, N_x, N_y and N_z denote the numbers of grid points in the x, y and z directions, respectively, and, Δx^+, Δy^+ and Δz^+ are the dimensionless collocation grid spacings in the x, y and z directions, respectively. Since the velocity field is dealiased in the x and z directions, the effective grid spacings in those directions are larger than the collocation grid spacings by the factor 1.5. The grid points in the x and z directions are evenly spaced. In the y direction, the grid points are not evenly spaced. Since Chebyshev polynomials are used in the y direction, the grid points are given by the Chebyshev collocation points, which are more closely spaced near the channel walls. For the low Reynolds number channel reported in Part II, the grid spacings are the same as those used by McLaughlin (1989).

In general, one could use different time steps for the integration of the fluid and particle equations of motion. However, the time step used in the simulations in Part II was 0.25 time wall units for both the fluid and the droplets. The time step is determined by considerations of stability and accuracy. Lyons et al. (1991) found that $\Delta t^+ = 0.25$ provided sufficient accuracy for the time integration of the fluid velocity field in the channel and that the time integration was numerically stable. When one is tracking small particles, one should also consider the particle relaxation time when determining a suitable time step. If $\Delta t^+ > \tau^+$, one might expect that the trajectories of the particles would be inaccurate. However, if $\tau^+ < 1$, the particles move with the surrounding fluid to a good approximation. Thus, in this case, provided that the time step is small enough to accurately simulate the channel flow, it should also suffice for the particle calculations. Table 4 shows that Runs 3 and 8 violated the condition $\Delta t^+ \ll \tau^+$. However, when the runs were repeated with $\Delta t^+ = 0.125$, the results for the collision rates were the same within the statistical uncertainty.

If the particle motion is predominately controlled by Brownian motion, the time step should be small enough that the Brownian root-mean-square displacement over a time step should be smaller than the grid spacing. This ensures that the coupling between Brownian motion and the small scales of turbulence is captured. However, for the high Sc numbers in Table 4, the contribution of Brownian motion is expected to be negligible.

Finally, a time step much smaller than the mean time between collisions, τ_c, is required to prevent multiple collisions of a single particle within a time step, which the current algorithm would not account for.

The simulation of the particle phase introduces additional numerical parameters. The number of droplets, N_p, released at the initial time is determined by the initial number concentration and the size of the computational domain:

$$N_p = C_0^+ L_x^+ 2h^+ L_z^+, \tag{49}$$

where

$$C_0^+ = C_0 l^{*3} \tag{50}$$

is the number of particles in a wall volume unit. For the runs carried out in Part II, N_p varied in the range 50,000–300,000. Previous work by Kontomaris et al. (1992) has shown that about 8000 particle trajectories suffice for accurate single particle Lagrangian statistics. When the

determination of the average collision rate is sought, a sufficient number of particles is required to obtain a statistically significant collision rate over a given run. Therefore, for slowly colliding small droplets a large number of droplets must be traced. However, if the monodispersity of the suspension must be approximately preserved over the duration of a run, the number of droplets must be restricted to small values. This would be the case for rapidly colliding large droplets. Furthermore, the number of droplets should be limited to a range where the omission of feedback effects does not compromise the accuracy of the results. Finally, the feasible number of droplets is limited by the available computational memory and speed.

The collision search lattice requires the specification of the number of slices of the computational domain, κ_x and κ_z. The size of a slice in the downstream and spanwise directions has to be sufficiently large that collisions between particles originating from locations more than one slice apart (in the both x and z directions) are unlikely over the duration of a time step ($\Delta t^+ = 0.25$.) An appropriate constraint on the slice widths ΔL_x^+ and ΔL_z^+ is that they exceed twice the distance that two particles are likely to move relative to each other over a time step:

$$\frac{\Delta L_x^+}{2} > |\Delta v_x^+| \Delta t^+, \tag{51}$$

$$\frac{\Delta L_z^+}{2} > |\Delta v_z^+| \Delta t^+. \tag{52}$$

The relative velocities of small particles can be estimated as

$$|\Delta v_x^+| \approx (2)^{1/2} u_x'^+, \tag{53}$$

$$|\Delta v_z^+| \approx (2)^{1/2} u_z'^+, \tag{54}$$

where u'_x and u'_z are the root-mean-square values of the fluid velocity fluctuations. Any correlation in the motion of neighboring particles would reduce their relative velocity. In the core of the channel, turbulence intensities are expected to be of order 1 wall unit. The streamwise intensity reaches a value of about 2.5 in the vicinity of the wall. Therefore, the constraints on ΔL_x^+ and ΔL_z^+ become $\Delta L_x^+ > 1.77$ and $\Delta L_z^+ > 0.71$. The channel used in Part II was divided into 16×64 slices. The size of each slice in wall units was $(630/16) \times 250 \times (630/64)$ or $39.38 \times 250 \times 9.84$ in the downstream (x), normal (y), and spanwise (z) directions.

A final computational parameter that one must select is the duration of a run, T_f. There are a number of factors that one must consider in selecting this parameter. First, T_f should be larger than the largest time scales that must be studied. If the typical behavior of a phenomenon is influenced by the large turbulence eddies in the channel core, T_f must be larger than T^E, where T^E is the Eulerian integral time scale in the core. The characteristic time of the wall eddies is 100 wall time units. Allowing the simulation to proceed over several eddy turnover times permits each droplet to sample a variety of velocity fluctuations that are typical of the turbulent channel flow.

It is also desirable that the simulation time be large compared to the particle relaxation time, τ, to allow the particles to become fully entrained in the surrounding fluid and to eliminate the effect of their initial velocity. Finally, collision statistics must be collected over times large relative to the mean free time between collisions of a single particle, τ_c. This constraint can be examined at the end of a run after the mean collision time has been determined.

Other considerations, however, may limit the desired run time. For example, the primary goal pursued in Part II was to determine the collision rate between identical droplets. Since droplets coalesce upon collision, the duration of the run was limited to the early stages of evolution while the suspension of droplets remained nearly monodisperse. Furthermore, an approximately constant and uniform droplet concentration distribution was desirable over the time that collision statistics were collected to simplify the interpretation of the results. Therefore, the duration of a run was limited to the early stages of evolution while particle segregation near the channel walls, as discussed by Chen and McLaughlin (1995), and droplet deposition did not significantly modify the initially uniform droplet distribution. Since the rate of deposition increases with droplet relaxation time, channel depletion is most severe for the droplets with the largest relaxation times.

The duration of all runs in Part II except Run 23 was 100 wall time units. This was a compromise between the desire to sample several eddy turnover times and the desire to maintain a constant concentration profile and a monodisperse particle size distribution. This time is sufficient to permit the droplets to reach equilibrium with the surrounding fluid for $\tau^+ \ll 100$. Run 23, however, for the droplets with $\tau^+ = 50$, was extended for 300 wall time units.

4. Accuracy of computed collision rates

The accuracy of the computed collision rates must be assessed. Potential sources of error include inadequate resolution of the Eulerian flow fields, time-stepping errors in integrating the particle equation of motion, unaccounted multiple collisions of a given particle within the same time step, unaccounted collisions due to inadequate search grid spacing, and statistical errors due to a limited number of collisions.

4.1. Effect of flow resolution

The numbers of grid points in the x, y, and z directions were 16, 65 and 64, respectively. A few simulations were carried out with larger numbers of grid points in each direction. The results showed that the above resolution provided adequate accuracy for the collision rates.

4.2. Effect of velocity interpolation

The effect of interpolation accuracy on collisions was studied by comparing simulations in which PHI was used with simulations in which DS was used. Table 6 gives the total number of collisions over the simulation time, N_c, for two values of τ^+. For the $\tau^+ = 1.4$ droplets, the

Table 6
Effect of interpolation methods on collisions

ϕ_0	m_l	τ^+	d^+	ρ_p/ρ_f	Interpolation method	N_c
6.52×10^{-5}	6.48×10^{-3}	1.4	0.498	100.0	DS	439
					PHI	374
					Difference	−14.8%
1.56×10^{-4}	0.111	28	0.84	713.0	DS	3383
					PHI	3466
					Difference	2.45%

droplet–fluid density ratio was chosen to be 100.0. This makes d^+ sufficiently large to obtain statistically significant numbers of collisions. For the $\tau^+ = 28$ droplets, the density ratio was 713. For both case, the simulation time was 100 wall time units. The initial volume fractions were 6.52×10^{-5} and 1.56×10^{-4}, respectively, for the $\tau^+ = 1.4$ and $\tau^+ = 28$ droplets. The corresponding mass fractions were 6.48×10^{-3} and 0.111. At the initial time, the droplets were randomly distributed throughout the channel. The Reynolds number of the channel flow was 7050.

The results in Table 6 indicate that the errors caused by PHI are considered acceptable for the purposes of this paper. The largest errors are for the droplets with the smallest values of τ^+ since these droplets are affected most strongly by the smallest eddies. The interpolation errors for these droplets are comparable with the statistical uncertainty in the collision rate. In what follows, the results presented were obtained by using PHI, which is computationally 20 times cheaper than DS.

4.3. Time-stepping errors

When the time step used in the integration of the equation of particle motion is not sufficiently smaller than the particle relaxation time, significant errors could accumulate in the calculation of the particle trajectories and the number of collisions. However, the effect of such errors on the calculations to be reported in Part II was small. Table 7 shows the simulation results for the droplets of $\tau^+ = 0.126$ (Run 3). This is the smallest τ^+ used in this paper. The simulation time was 100 time wall units. All collisions occurring in the channel were counted during the indicated time period. The difference in the numbers of collisions is within statistical uncertainty. This is consistent with the idea that, when $\tau^+ < 1$, the droplets follow the fluid well and, provided that the time step is small enough to accurately simulate the channel flow, it should also suffice for the particle calculations.

Table 7
Effect of time step on collisions

τ^+	d^+	ρ_p/ρ_f	Δt	N_c
0.126	0.271	30.0	0.125	137
0.126	0.271	30.0	0.25	145

4.4. Unaccounted multiple collisions

The likelihood of multiple collisions per particle within a time step can be assessed after the mean time between successive collisions, τ_c, of a single particle has been determined. It must be ensured that the time step was sufficiently smaller than τ_c so that the collision rate was not significantly underestimated.

4.5. Unaccounted collisions between remote particles

The likelihood of collisions between particles originating outside the selected search neighborhood can be assessed after the particle mean free path, λ_c, has been determined. It must be ensured that the spacing of the collision search grid was sufficiently larger than λ_c so that the collision rate was not significantly underestimated.

4.6. Statistical accuracy of collision rates

When computing collision rates in specific volumes, it was necessary to choose sufficiently large volumes that statistically significant numbers of collisions could be obtained. A rough estimate of the statistical uncertainty in the collision rate can be obtained from the reciprocal of the square root of the number of collisions in a given volume. This requirement was especially severe for small values of τ^+. For this reason, it was not possible to determine the collision rate as a function of distance from the closest wall for $\tau^+ < 1$.

4.7. Verification against a known solution

Smoluchowski (1917) provided a simple mechanism to describe collision rates in uniform shear flow. The collision rate for monodisperse particles was expressed as

$$Z = \frac{2}{3} C^2 d^3 G, \tag{55}$$

where $G = \mathrm{d}U/\mathrm{d}y$ was the uniform shear rate.

To test the collision algorithm employed in this work, the simulation results obtained from a laminar flow are compared with (55). In the simulation, the fluid velocity was:

$$\mathbf{U}(y) = 16u* (1 - \exp[(y^2 - 2hy)/(32hl*)])\hat{x}. \tag{56}$$

The velocity profile in (56) roughly fits the mean velocity observed from the turbulent channel flow used in this work. Fig. 6 compares the simulation results with the collision rate obtained from (55). In Fig. 6, $u* = 75$ cm/s, $l* = 20$ μm and $t* = 26.67$ ms were used. The calculation was done for 16.8 μm olive oil droplets. The droplets were assumed to coalesce on impact. The bin width in calculating the collision rate of the simulation results was 1 wall unit (20 μm). The simulation results are consistent with Smoluchowski's theoretical prediction. The discrepancies in the channel center were caused by the small number of collisions. Since the shear rate in the channel center is very small, the number of collisions in each bin is of order

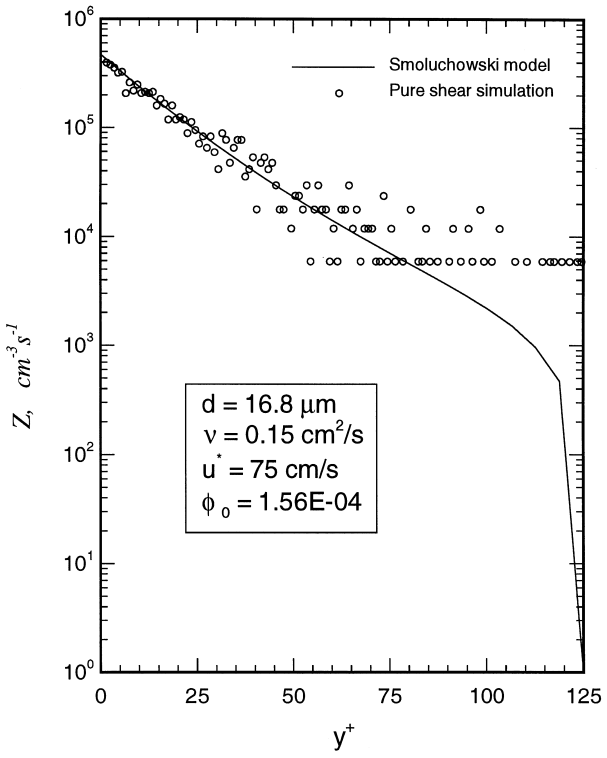

Fig. 6. Comparison of simulation results with Smoluchowski's theoretical predictions for a laminar shear flow.

unity. Close to the wall, where the shear rate is largest, the computed collision rates are in good agreement with Smoluchowski's theory.

5. Computational requirements

5.1. Memory

The memory requirements are mainly determined by the Reynolds number of the channel flow and the number of particles that are tracked. The number of grid points needed to adequately resolve the channel flow increases with the Reynolds number. For isotropic homogeneous turbulence, the Kolmogorov theory suggests that the number of grid points increases as $Re^{9/4}$. Thus, doubling the Reynolds number increases the resolution requirements by roughly a factor of 5.

In most of the computations that will be discussed in this paper, particle tracking required more memory than the channel flow simulation. One needs one dimensional arrays for each particle coordinate, each component of the particle velocity, and each component of the undisturbed fluid velocity at the particle locations. Furthermore, the values of the particle coordinates, each component of the particle velocity, and each component of the

undisturbed fluid velocity must be stored for the previous two time steps for the time-stepping procedure.

If the collision algorithm is efficiently implemented, it requires only a small fractional increase in the memory requirements.

5.2. CPU time

There are three main contributors to the CPU time used by the simulations. They are the simulation of the flow field, particle tracking, and collision detection. The CPU times presented in this section were obtained with the SGI Power Challenge computers at NCSA. Since there are several computers in the Power Challenge, the numbers may be affected by the particular machine that the program is run on and the loading on the machine at the time of execution.

For a fixed numerical channel, the CPU time for the simulation of the flow field is fixed. For the numerical channel used in this work, the CPU time used for simulating the turbulent flow field was 5.4 sec per time step. The CPU time used for particle tracking is proportional to the number of particles. If one tracks 50,000 particles, the CPU time used for particle tracking is 61 sec per time step. The CPU time used for collision detection is proportional to the square of particle numbers. If one has 50,000 particles in the channel, the CPU time used for collision detection is 245 sec per time step for the collision search grid used in this work.

It is clear that the simulation of the flow field takes a negligible part of the total CPU time. If one simulates more than 50,000 particles, collision detection uses the major part of the CPU time.

6. Conclusion

Part I of this paper described a method for simulating the behavior of small coalescing droplets in a turbulent channel flow. A novel aspect of the method was the incorporation of interdroplet collisions. The various input parameters, guidelines for their specification, and the accuracy of the computed collision rates were discussed. Part II reports collision statistics over a wide range of conditions.

Acknowledgements

The authors thank Mr S. Ramarajan for carrying out the high resolution tests. The authors wish to acknowledge the support and facilities of the National Center for Supercomputing Applications at the University of Illinois at Urbana. The authors also acknowledge financial support for this project by DuPont and Clarkson's Center for Advanced Materials Processing (CAMP). This material is based upon work supported in part by the New York State Science and Technology Foundation. Many of the techniques used in this work were developed with support from Dr Robert Price's program at the United States Department of Energy under contract DE-FG02-88ER13919.

References

Balachandar, S., Maxey, M.R., 1989. Methods for evaluating fluid velocities in spectral simulations of turbulence. J. Comput. Phys. 83, 96–125.

Chen, M., McLaughlin, J.B., 1995. A new correlation for the aerosol deposition rate in vertical ducts. J. Colloid Interface Sci. 169, 437–455.

Chen, M., Kontomaris, K., McLaughlin, J.B., 1995. Dispersion, growth, and deposition of coalescing aerosols in a direct numerical simulation of turbulent channel flow. Gas–Particle Flows 228, 27–32.

Clift, R., Grace, J. R., Weber, M. E. 1978. Bubbles, Drops and Particles. Academic Press, New York.

Hogue, C., Newland, D., 1994. Efficient computer simulation of moving granular particles. Powder Technol. 78, 51–66.

Hopkins, M.A., Louge, M.Y., 1991. Inelastic microstructure in rapid granular flows of smooth disks. Phys. Fluids A 3, 47–57.

Kontomaris, K., Hanratty, T.J., McLaughlin, J.B., 1992. An algorithm for tracking fluid particles in a spectral simulation of turbulent channel flow. J. Comput. Phys. 103, 231–242.

Lavieville, J., Deutsch, E., Simonin, O., 1995. Large eddy simulation of interactions between colliding particles and a homogeneous isotropic turbulent field. Gas–Particle Flows 228, 347–357.

Lyons, S.L., Hanratty, T.J., McLaughlin, J.B., 1991. Large-scale computer simulation of fully developed channel flow with heat transfer. Int. J. Numes. Meth. Fluids 13, 999–1028.

Marble, F.E., 1964. Mechanism of particle collision in the one-dimensional dynamics of gas-particle mixtures. Phys. Fluids 7, 1270–1280.

McLaughlin, J.B., 1989. Aerosol particle deposition in numerically simulated channel flow. Phys. Fluids A 1, 1211–1224.

McLaughlin, J.B., 1994. Numerical computation of particles–turbulence interaction. Int. J. Multiphase Flow 20, 211–231.

Saffman, P.G., 1965. The lift on a small sphere in a slow shear flow. J. Fluid Mech. 22, 385–400.

Saffman, P.G., Turner, J.S., 1956. On the collision of droplets in turbulent clouds. J. Fluid Mech. 1, 16–30.

Smoluchowski, M. Z., 1917. Versuch einer mathematischen theorie der koagulationskinetic kolloider losungen. Phys. Chem. 92, 129.

Sundararajakumar, R.R., Koch, D.L. 1996. Non-continuum lubrication flows between particles colliding in a gas. J. Fluid Mech. 313, 283–308.

Sundaram, S., Collins, L.R., 1994. Collision statistics in particle-laden isotropic turbulence. AIChE Annual Meeting, San Francisco.

Sundaram, S., Collins, L.R., 1996. Numerical considerations in simulating a turbulent suspension of finite-volume particles. J. Comput. Phys. 124, 337–350.

Sundaram, S., Collins, L.R., 1997. Collision statistics in an isotropic, particle-laden turbulent suspension. Part I. Direct numerical simulations. J. Fluid Mech. 335, 75–109.

Yeung, P.K., Pope, S.B., 1988. An algorithm for tracking fluid particles in numerical simulation of homogeneous turbulence. J. Comput. Phys. 79, 373–416.